Materials Today Bio 16 (2022) 100387

Contents lists available at ScienceDirect

Materials Today Bio

journal homepage: www.journals.elsevier.com/materials-today-bio

Enhanced sciatic nerve regeneration by relieving iron-overloading and organelle stress with the nanofibrous P(MMD-co-LA)/DFO conduits

Lei Han [a,1], Xianzhen Dong [a,1], Tong Qiu [a,*], Zhaona Dou [a], Lin Wu [a], Honglian Dai [a,b,**]

[a] State Key Laboratory of Advanced Technology for Materials Synthesis and Processing, Biomedical Materials and Engineering Research Center of Hubei Province, Wuhan University of Technology, Wuhan, 430070, China

[b] Foshan Xianhu Laboratory of the Advanced Energy Science and Technology Guangdong Laboratory, Xianhu Hydrogen Valley, Foshan, 528200, China

ARTICLE INFO

Keywords:
Peripheral nerve regeneration
Wallerian degeneration
Iron overload
Mitochondria stress
Endoplasmic reticulum stress

ABSTRACT

Wallerian degeneration after peripheral nerve injury (PNI), that is, the autonomous degeneration of distal axons, leads to an imbalance of iron homeostasis and easily induces oxidative stress caused by iron overload. Inspired by the process of nerve degeneration and regeneration, the design of a functional electrospinning scaffold with iron chelating ability exhibited the importance of reconstructing a suitable microenvironment. Here, an electrospinning scaffold based on deferoxamine and poly(3(S)-methyl-morpholine-2,5-dione-*co*-lactone) (PDPLA/DFO) was constructed. This work aims to explore the promotion of nerve regeneration by the physiological regulation of the scaffold. *In vitro*, PDPLA/DFO films mitigated the reduction of glutathione and the inactivation of Glutathione peroxidase 4 caused by iron overload. In addition, they decreased reactive oxygen species, relieve the stress of the endoplasmic reticulum and mitochondria, and reduce cell apoptosis. *In vivo*, PDPLA/DFO conduits constructed the anti-inflammatory microenvironment and promoted cell survival by alleviating iron overload and organelle stress. In conclusion, PDPLA/DFO guidance conduits targeted the distal iron overload and promoted nerve regeneration. It provides novel ideas for designing nerve conduits targeting the distal microenvironment.

1. Introduction

Peripheral nerve injury (PNI) is a common traumatic disease that can cause sensory and motor dysfunction, and delayed treatment may cause permanent disability [1,2]. The disturbance of neuronal regeneration microenvironment is associated with delayed regeneration and insufficient functional recovery. It is reported that iron content and iron uptake of the distal stump increased after PNI [3]. To some extent, iron is essential for normal neuronal function, while there have been many researches showing that neurodegenerative diseases are related to iron overload [4]. Iron exists in the body in the form of iron-containing compounds such as hemoglobin (65%), transferrin (15%), coenzymes or prosthetic groups as well as ferritin and hemosiderin [5,6]. RBCs respond to nerve injury and aggregate, so distal nerves are enriched in large amounts of hemoglobin [7]. In addition, up-regulation of transferrin expression also caused iron enrichment [8]. These are thoughts to be the main causes of iron homeostasis imbalance after nerve injury. Excess iron causes an increased production of reactive oxygen species leading to cell dysfunction or death, tissue damage and organ disease [9]. Iron overload has been shown to promote apoptosis of osteoblasts, chondrocytes, cardiomyocytes and liver cells by inducing endoplasmic reticulum (ER) stress or mitochondrial dysfunction [10–12]. However, the effect of iron overload on peripheral nerves is rarely studied.

Pathologically, ER dysfunction is involved in neuronal degeneration in several human diseases, such as Alzheimer's disease and Parkinson's disease. Also, several lines of evidence support the contribution of unfolded protein reaction branches to axonal injury events. Loureirin B promoted nerve regeneration after spinal cord injury (SCI) by inhibiting ER stress and mitochondrial dysfunction [13]. Vitamin B12 improved neurological functional recovery after traumatic brain injury by down-regulation of the endoplasmic reticulum stress-related apoptosis signaling pathway [14]. Mitochondria play an essential role in neuronal function, vital for ATP production as well as Ca^{2+} buffering capacity, and cellular signaling. Loreto et al. indicated that mitochondrial impairment

* Corresponding author.
** Corresponding authorState Key Laboratory of Advanced Technology for Materials Synthesis and Processing, Biomedical Materials and Engineering Research Center of Hubei Province, Wuhan University of Technology, Wuhan, 430070, China.
E-mail addresses: tongttqq@whut.edu.cn (T. Qiu), daihonglian@whut.edu.cn (H. Dai).
[1] Lei Han and Xianzhen Dong are co-first authors.

https://doi.org/10.1016/j.mtbio.2022.100387
Received 31 May 2022; Received in revised form 24 July 2022; Accepted 25 July 2022
Available online 6 August 2022

replicated all the significant steps of WD, potentially contributing to axon pathology in mitochondrial disorders [15]. Iron homeostasis is also connected with ER and mitochondrial damage. Acute cadmium exposure activated the ER stress, which is likely activated by Mito-ROS, resulting in iron death [16]. Peroxiredoxin 5 prevented iron overload-induced neuronal death by inhibiting mitochondrial fragmentation and ER stress [17]. Organelle stress is related to iron overload in PNI, and affects nerve regeneration.

Conventional neural-supporting scaffolds fail to restore neural structure and function due to the inability to reconstruct the unbalanced microenvironment. It is incredibly significant to consider the major microenvironmental cues during peripheral nerve regeneration (PNR) when designing and fabricating functionally biomimetic nanomaterials and related supporting scaffolds [18]. Many efforts have been devoted to regulating inflammation, oxidative stress or organelle function. For instance, nanodiamond/polycaprolactone (PCL) nerve bridges ameliorate the immune milieu by inducing M1 to M2 macrophage polarization, which exhibits similar repair capabilities as autografts [19]. 3D manufacture of melatonin/polycaprolactone nerve guide conduit ameliorated immune milieu by reducing oxidative stress, inflammation and mitochondrial dysfunction [20]. Wallerian degeneration (WD) occurs at the distal portion of a nerve fiber early after peripheral nerve injury [21], which regulates the distal microenvironment. During this process, Schwann cells remove the fragments of myelin produced by disintegrating axons, and the microenvironment changes subsequently [22]. Focusing on WD is meaningful for nerve regeneration.

The adoption of materials is a prerequisite element of periphery nerve tissue engineering. Generally, polyester materials such as poly(lactic-*co*-glycolic acid) (PLGA), poly-ε-caprolactone (PCL) and poly(L-lactic acid) (PLLA) possess favourable biocompatibility and biodegradability [23]. However, their implantation will disturb the pH of the microenvironment. Amino acid modification is capable of limiting acid degradation and inhibiting the generation of aseptic inflammation, which is a suitable solution. For example, the colymers of p(MMD-*co*-LA), p(MMD-*co*-GA), p(MMD-*co*-CL) based on the polymerization of 3(S)-methyl morpholin-2, 5-dione (MMD) with lactide, glycolide and caprolactone are common nerve fiber scaffolds for tissue engineering [24]. In particular, the excellent biodegradability of p(MMD-*co*-LA) determines the comprehensive application. In addition, electrospinning technology is regarder as the efficient method for manufacturing nanofiber scaffolds with interconnected pores, high porosity and large surface area, which is conducive to drug loading and controlled release [25]. Hence, p(MMD-*co*-LA) prepared by electrospinning is an ideal nerve guidance conduit. Nevertheless, nerve regeneration is hindered by iron overload. Deferoxamine (DFO) is the most widely used iron chelator in clinical practice, which can safely and effectively relieve iron overload [26–28]. The reliable protective effect of DFO has attracted the attention of researchers, because it can anchor free iron to reduce iron overload in the affected area. Herein, we prepared DFO-loaded p(MMD-*co*-LA) conduits (PDPLA) in order to resolve abnormal increase of distal iron content (Scheme 1). Subsequently, we evaluated the conduits to relieve iron overload *in vitro* and repair PNI *in vivo*.

2. Materials and methods

2.1. Preparation and characterization of PDPLA/DFO conduits

2.1.1. Preparation of PDPLA/DFO conduits

Weighed 1 mol of L-alanine (LA, Sigma-Aldrich, USA) and dissolved it in 300 mL of 4 mol/L sodium hydroxide (Sinopharm Chemical Reagent, China) solution. The above-mentioned L-alanine solution (−13 °C precooling) was added dropwise 250 mL of chloroacetyl chloride (Sinopharm Chemical Reagent, China) in dichloromethane solution (1 mol/L) and 250 mL of sodium hydroxide solution (4 mol/L). After the reaction was complete, the supernatant was extracted three times with 200 mL of ethyl acetate and titrated to pH = 1 by adding hydrochloric acid. The *N*-chloroacetyl-L-alanine was obtained by removal of the solvent. Weighed 20 g of *N*-chloroacetyl-L-alanine and dissolved it in 100 mL of dimethylformamide (DMF, Sinopharm Chemical Reagent, China) solution. After 30 mL of triethylamine was reacted with the above solution (anhydrous and oxygen-free, constant temperature 95 °C), put it at −20 °C, take the supernatant and remove the solvent to obtain 3(S)-methylmorpholine-2, 5-dione (MMD).

P(MMD-co-LA) was prepared by ring-opening polymerization of LA and MMD. In brief, weighed 4 g of MMD and 12 g of LA into the reaction tube, and added 3.2 ml of 1% (w/v) $Sn(Oct)_2$ (Sigma-Aldrich, USA) chloroform solution. Then, after cooling with liquid nitrogen for 25 min, the tube was evacuated and sealed. The reaction tube was placed in an oil bath at 140 °C for 16 h, all the reaction products were dissolved in chloroform and rotary-evaporated, which was repeated three times to remove impurities. Subsequently, it was freeze-dried under vacuum to prepare P(MMD-*co*-LA) powder.

The prepared P(MMD-*co*-LA) powder (2 g) was dissolved in 10 mL of 1,1,1,3,3,3-hexafluoro-2-propanol (Aladdin, China) solvent to prepare 20% (w/v) P(MMD-*co*-LA) solution. In addition, 10 mg of DFO was added to 5 mL of the P(MMD-co-LA) solution. Put the P(MMD-*co*-LA) (PDPLA) and P(MMD-*co*-LA)/DFO (PDPLA/DFO) spinning dope into a 10 mL standard syringe with a 22-gauge stainless steel needle. Electrospinning uses a high voltage of 9 kV (Beijing Yongkang), a flow rate of 0.6 mL h^{-1}, and a high-speed (2800 rpm) collecting drum with tin foil to maintain a distance of 15 cm from the electrode. After freeze-drying, the harvested fiber membranes were named PDPLA and PDPLA/DFO respectively. The PDPLA and PDPLA/DFO fiber membranes were rolled into cylindrical to prepare nerve grafts.

2.2. Characterization of fiber films

AMX-500 NMR spectrometer (Bruker, Germany) was used to detect the DMSO solution's ^1H NMR spectrum of P(MMD-*co*-LA). Evaluated the surface morphology of fiber films by scanning electron microscope (SEM, JSM-IT200, JEOL, Japan), and used ImageJ software (v1.8.0, NIH, USA) to determine the fiber diameter. The mechanical properties of the fiber films were tested by an electronic universal material testing machine (Instron 5967, Instron Corporation, USA). Three sets of parallel samples were set for each characterization.

Prepared DFO solutions of various mass concentrations (1.0, 2.0, 4.0, 8.2, 16.5, 31.6,60.4, 121.7, 250.1, 500.0 μg/mL) and chelated them with excess $FeCl_3$ in a volume ratio of 9:1 respectively. Absorbance at 485 nm, measured by a microplate reader, drew the standard curve of DFO. Soak 100 mg of P(MMD-*co*-LA)/DFO membrane in 10 mL of PBS solution and place it in a shaker at 37 °C. Take out 0.9 mL of release medium at specific time points (1 h, 2 h, 4 h, 8 h, 16 h, 24 h, 36 h, 48 h, 60 h, 72 h, 7th day, 14th day, 21st day, and 28th day) and respectively add them to 0.1 mL $FeCl_3$ solution. After mixing well, measure the absorbance at 485 nm with a microplate reader to determine the release rate of DFO. Utilized equal volume of PBS to maintain system balance.

2.3. Cell culture

Rat Schwann cells (RSCs) (American Type Culture Collection, ATCC) were cultured in Dulbecco's modified Eagle medium (DMEM, Hyclone) supplemented with 10% (v/v) fetal bovine serum (FBS, Gibco, USA), 100 U/mL penicillin and 100 U/mL streptomycin at 37 °C in 5% CO_2 humidified air.

2.4. In vitro study

2.4.1. Explant culture and iron staining

Explants, which is the nerves cultured *in vitro*, undergo a process similar to Wallerian degeneration [29,30]. Explant cultures were used to detect iron overload during WD. In brief, sciatic nerves were removed from the rat and divided into 3–4 mm segments. Then, the nerve

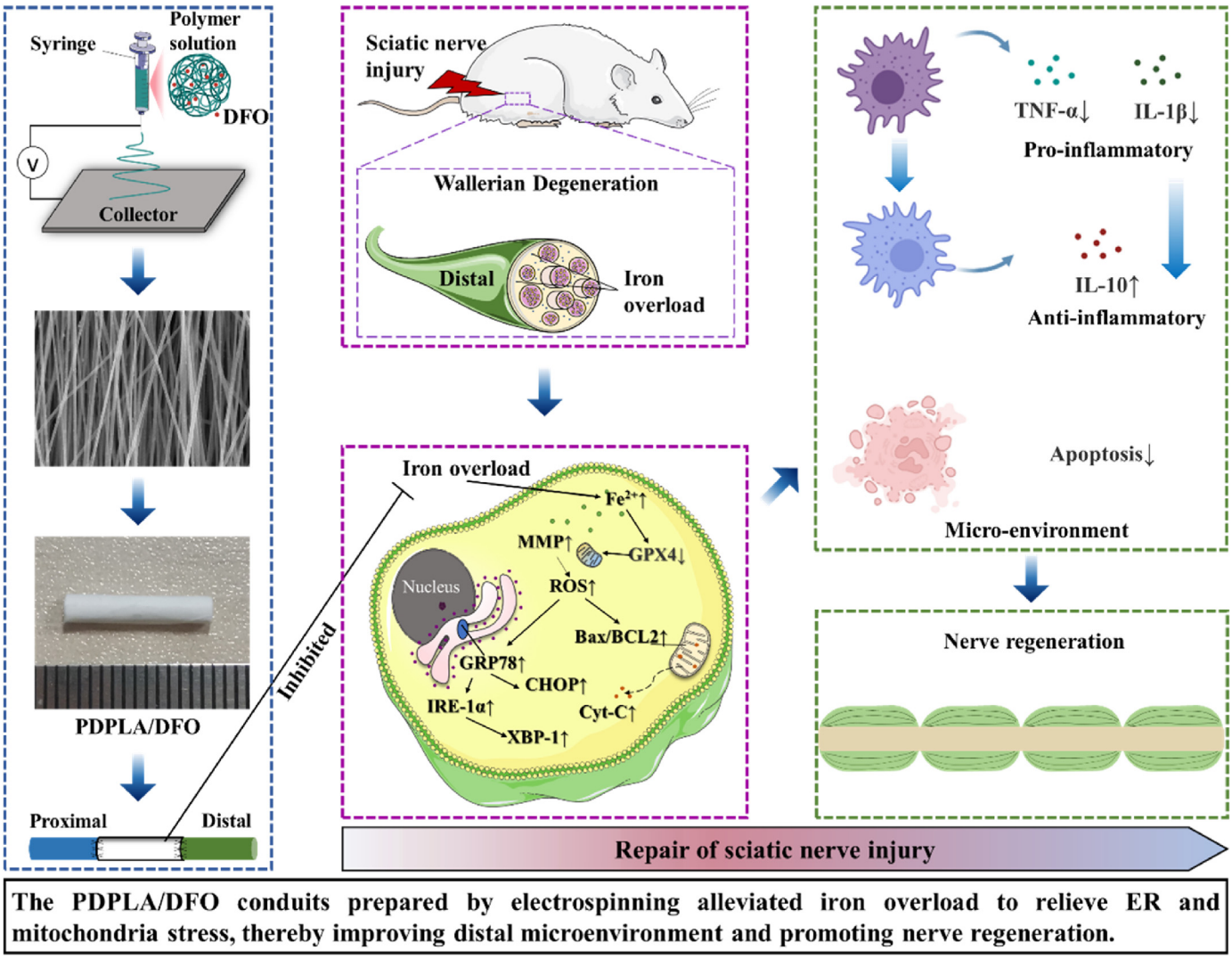

Scheme 1. The PDPLA/DFO nerve guidance conduits synthesized by electrospinning repair peripheral nerve injury.

segments were cultured in serum-free DMEM at 37 °C, 5% CO_2. After 0 (control), 1, 3 and 5 days, the explant sections were stained with Perl's dye (Repeat each group three times, n = 3). Perl's staining is a sensitive and traditional method for visualizing iron content in tissues by separating ferric ions from proteins using dilute hydrochloric acid and forming blue precipitates with potassium ferrocyanide, while the nuclei are restained with eosin [31,32]. Therefore, the experiment visually assessed the distribution of ferric iron in the sciatic nerve during WD.

2.4.2. Cell viability assay

Cell viability was determined by Cell Counting Kit-8 (CCK-8, Beyotime, Shanghai, China) assay. RSCs were seeded in 96-well plates with a density of 5×10^3 cells/well. After incubation one day, cells were treated with 2.5, 5, 10 and 20 mM ferric ammonium citrate (FAC, MW = 488.1, purity = 99.5%) solution for 24 h (n = 3). Then, 10% of CCK-8 was added to the culture medium and incubated for 2 h at 37 °C. The plate was measured at 450 nm by using the microplate reader (Thermo Fisher Scientific, USA).

2.4.3. Intracellular labile iron pool (LIP)

The Calcein-acetoxymethyl ester (Calcein-AM, 1 μM) was used to analyze the relative changes of cellular labile iron (n = 3). RSCs were inoculated in a 6-well plate at a density of 2×10^5 cells/mL, collected after 2.5, 5, 10 and 20 mM FAC treatment for 24 h and washed with PBS, stained with 1 mL of 1 μM Calcein-AM for 30 min at 37 °C in the dark. The cells were imaged by an inverted fluorescence microscope (Olympus, DP72, Japan).

2.4.4. Detection of glutathione (GSH), glutathione peroxidase 4 (GPX4)

As treated as described above, the harvested cells were washed with PBS and lysed with cell lysate (Beyotime, Shanghai, China) (n = 3). After centrifugation, the supernatant content of GSH was detected by GSH and GSSG detection kit (Beyotime, Shanghai, China), and the activity of GPX4 was detected by Rat glutathione peroxidase 4 (GPX4) ELISA kit (Ruiyu bio, shanghai, China).

2.4.5. Evaluation of mitochondrial membrane potential (MMP), reactive oxygen species (ROS) and apoptosis

MMP, ROS and apoptosis were detected by enhanced mitochondrial membrane potential detection kit with JC-1 (5,5,6,6-tetrachloro-1,1,3,3-tetrathylbenzimidazolyl-carbocyanine iodide) staining (Beyotime, Shanghai, China), ROS kit (Beyotime, Shanghai, China) and Annexin V-FITC/PI apoptosis detection kit (Beyotime, Shanghai, China), respectively (n = 3). In brief, PDPLA and PDPLA/DFO membranes were cut into several discs, which were sterilized by ultraviolet for 12 h and placed in a 96-well plate. RSCs were seeded on the membrane at a density of 2×10^5 cells/mL. After adherence, it was treated with medium with or without indicative FAC concentration for 24 h. Subsequently, the pre-treated cells

were stained with appropriate dye in the dark at 37 °C. After about 20–30 min, the dye solution was washed and the stained cells could be analyzed by an inverted fluorescence microscope (Olympus, DP72, Japan).

2.5. In vivo study

2.5.1. Animals and surgery

Male Wistar rats (180–250 g) were provided by the Hubei Provincial Center for Disease Control and Prevention (Wuhan, China). All animal tests were conducted in accordance with the protocol approved by the Hubei Medical Laboratory Animal Center (Permit number: SYXK (Hubei) 2019–0106). The rats were anesthetized using injection of pentobarbital (3.5 mg/100 g) into the abdominal cavity. Then sciatic nerve defects of 10 mm in rats were made and randomly filled with the following 4 groups (n = 3 for each): Control group, Autograft group, PDPLA group and PDPLA/DFO. The surgical incision was stitched by layers using absorbable sutures, and the experimental process is shown in Figure S2.

2.5.2. Histology staining

One week after surgery the rats were killed by an overdose of pure pentobarbital (50 mg/mL). For histopathological examination, the distal end (1.0 cm) of the injured sciatic nerve was harvested and fixed in 4% formalin for 24 h. Then, the tissues were embedded in paraffin and sliced into 4-μm-thick slices. After deparaffinization with xylene and hydrating with ethanol, the sections subjected to H&E (hematoxylin and eosin) and TB (toluidine blue) staining. Finally, the histopathological changes were observed with an optical microscope.

2.5.3. Ultrastructure observation by transmission electron microscope

Specimen for ultrastructure analyses was taken from the distal nerve portion, fixed in cacodylate buffer, osmicated, dehydrated, en-bloc stained with uranyl acetate, flat-embedded in Durcupan, and cut ultra-thin (50 nm) for transmission electron microscopy (FEI Tecnai G^2 20 TWIN, America) with 200 kV voltage.

2.5.4. Pathological analysis

For the immunohistochemistry, the sections were degreased with paraffin and covered with an antigen retrieval solution at 95~100 °C, then, blocked with 5% goat blocking serum for 30 min. Primary antibodies *Anti*-TNF-α (1:2000, Servicebio), *Anti*-IL-1β (1:1000, Servicebio), *Anti*-IL-10 antibody (1:1000, Servicebio), *Anti*-Bax (1:1500, Servicebio), *Anti*-BCL-2 (1:1500, Servicebio), *Anti*-Cyt-c (Cytochrome-c, 1:1000, Servicebio), *Anti*-CHOP (C/EBP homologous protein, 1:2000, Abdonal), *Anti*-IRE1-α (Inositol-requiring enzyme-1 alpha, 1:2000, Abdonal) and *Anti*-XBP1 (X-box binding protein 1, 1:2000, Abdonal) were used. Secondary antibodies goat *anti*-mouse IgG (1:200, Gibco) and the DAB substrate kit (Servicebio) were used. The slices were imaged by using an Olympus upright microscope (Olympus, DP71, Japan).

For immunofluorescence staining, the sections were permeabilized with 0.2% Triton X-100, 10% normal goat serum and 0.1% BSA in PBS for 1 h. Primary antibodies *Anti*-CD68 (1:1000, Servicebio), *Anti*-HO-1 (Heme oxygenase-1, 1:1000, Servicebio), *Anti*-GRP78 (glucose-regulated protein78, 1:1000, Servicebio) antibody were used. TRITC-labeled and FITC-labeled secondary antibody goat anti-mouse IgG (1:200, Gibco) were used. The sections were imaged by using an Olympus inverted fluorescent microscope (Olympus DP72, Japan).

2.5.5. Terminal-deoxynucleotidyl transferase mediated dUTP nick end labeling (TUNEL) assay

Cell apoptosis was measured with a TUNEL kit (Beyotime, Shanghai, China). The sections were incubated with proteinase K for 20 min and with H_2O_2 for 10 min. TUNEL reaction mixture was next applied to incubate with the sections in the darkness for 1 h. Next, sections were washed 3 times with phosphate buffer saline (PBS) and incubated using horse red peroxidase-streptavidin reagent (1:200) at room temperature. After 30 min, sections were washed 3 times with PBS and then counterstained with hematoxylin. The sections were imaged by using an Olympus inverted fluorescent microscope (Olympus DP72, Japan).

2.6. Semi-quantification of protein expression

We placed the sections under the microscope, and randomly selected 5 areas at 200x and photographed them (n = 3). Next, the positive sites of each immunohistochemical picture were selected. The integral optical density (IOD) and number of cells (n) were calculated with image j [33–35]. Average optical density value for a specific protein: OD = IOD/n. The relative protein expression of each group can be obtained by comparing the OD of other groups with the OD of the control group.

2.7. Assessment of sciatic nerve function recovery

The recovery of sciatic nerve function at 4 weeks postoperatively was assessed by walking trajectory and electrophysiological analysis. Rats were allowed to walk in one direction and left footprints on paper. Three parameters were measured from the animals' footprints: paw length, toe width, and middle toe width both non-surgically and post-experimentally. All data were measured with the experimenter unknown group (n = 3). Calculate the SFI value as previously described [24]. A ground electrode was fixed to the tail of the anesthetized rat. A 10 mV electrical stimulation was applied to the proximal sciatic nerve, and compound motor action potentials were recorded by placing a monopole in the gastrocnemius muscle.

2.8. Statistical analysis

All quantification data were presented as mean ± standard deviation(SD). Statistical analysis was carried out in OriginPro 2021 (OriginLab,USA). Statistics for multiple comparisons were performed using ANOVA or Student's t-test. A threshold of $p < 0.05$ was used to determine statistical significance.

3. Results and discussion

3.1. Characterization of fiber films

^{1}H NMR spectrum determined structure of final product (Fig. 1A). The characteristic resonance at 8.45 ppm indicated the presence of –NH–. Peaks of 1.33 ppm and 4.45 ppm represent methyl and methyl protons beside the carboxyl group, respectively. The characteristic resonance at 4.68 ppm was the methylene beside the amide bond. In addition, the characteristic formants at 1.55 ppm and 5.35 ppm were methyl peaks and methyl proton peaks near ester bonds. These results demonstrated that MMD and LA polymerized to P(MMD-*co*-LA). The integral ratio of the methyl peak area determined that the reaction ratio of MMD and LA was 1 : 2.66. Fig. 1B showed the release curve of DFO *in vitro*. Initially, DFO was released quickly, with a release rate of 29.0% ± 1.5% at 1 h and 39.0% ± 2.5% at 24 h. Subsequently, DFO was released uniformly and slowly, with a release rate of 60.2% ± 1.0% at 7 d and 95.0% ± 1.4% at 28 d. The property was conducive to maintain iron homeostasis after nerve injury. Fig. 1C illustrated aligned fibers of PDPLA and PDPLA/DFO. These fibers are uniform and continuous, with a diameter in the range of 400–1200 nm. The average diameter of PDPLA was 790 ± 190 nm, while that of PDPLA/DFO was 780 ± 150 nm. Fig. 1D showed tensile properties of the fiber membrane. The Young's moduli of $^+$PDPLA and $^+$PDPLA/DFO were 435.1 ± 41.0 MPa and 446.69 ± 14.80 MPa, respectively. It indicated that the fiber membranes have excellent tensile strength. The deformation rates of -PDPLA and -PDPLA/DFO were 202.4 ± 63.8% and 263.9 ± 13.1%, respectively. The results showed that the fiber membranes possessed outstanding ductility. Fig. 1E displayed live/dead staining, and Fig. 1F exhibited cell viability of RSCs on the membrane at

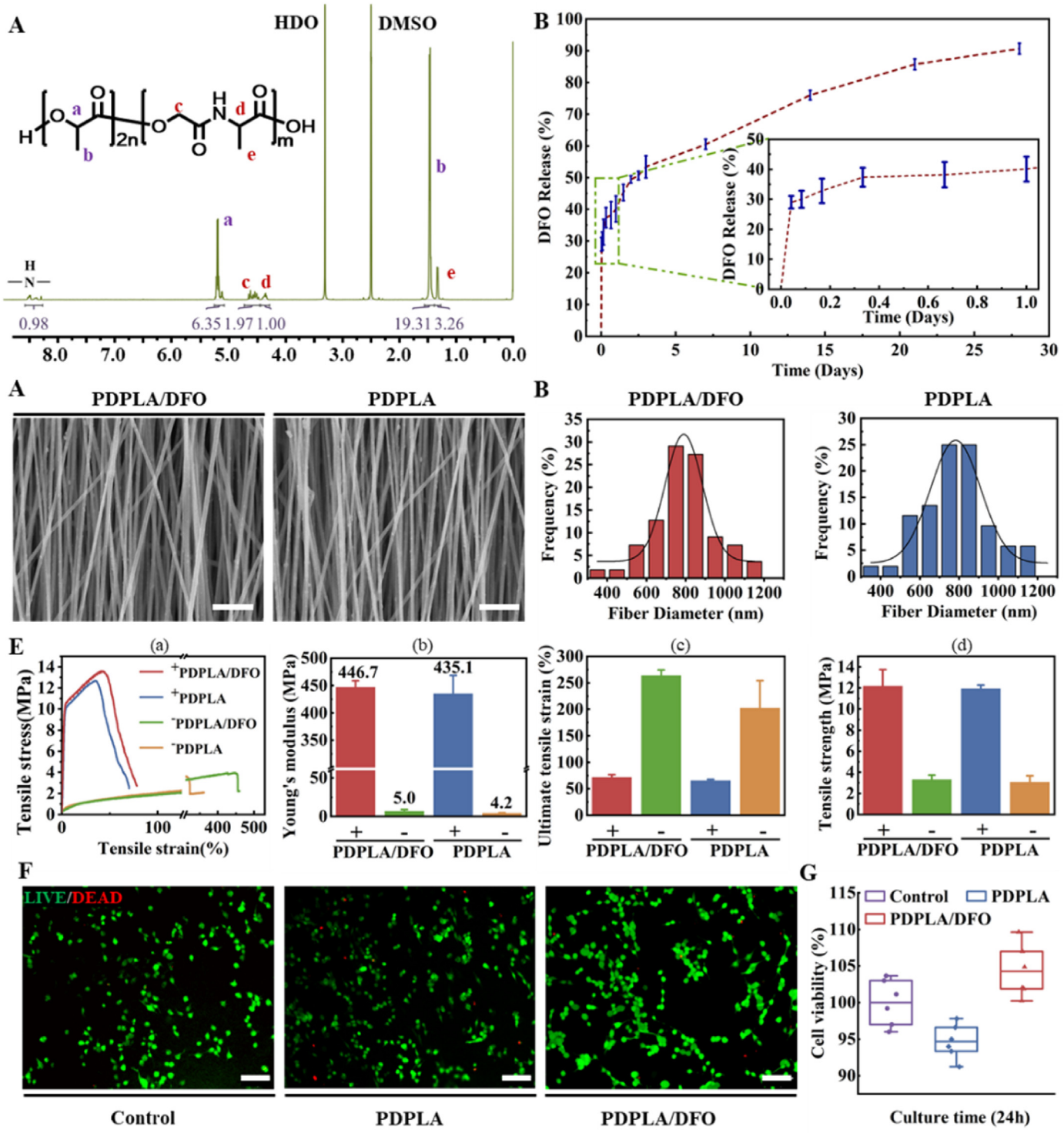

Fig. 1. Characterization of fiber membranes. (A) ^{1}H NMR spectra of P(MMD-*co*-LA). (B) Drug release curve of PDPLA/DFO. (C) SEM images of fiber film and (D) distribution diagram of fiber diameter of PDPLA and PDPLA/DFO. (E) Tensile property test of fiber membrane, "+" and "–" represent respectively parallel and perpendicular to the orientation of aligned fiber; (a) Strain stress curve, (b) Young's modulus, (c) Untimate tensile strain, (d) Tensile strengh. (E) LIVE/DEAD staining of RSCs seed on fiber films, scale bar = 100 μm. (F) Cell viability of RSCs on films was measured by CCK-8 (24 h). Data are means ± SD, n = 3, *p < 0.05.

24 h. The viability of RSCs on PDPLA/DFO electrospun films was significantly improved, which may be attributed to the pharmacological induction of hypoxia adaptation to promote the survival of transplanted RSCs [36]. The results showed that both PDPLA and PDPLA/DFO were suitable for adhesion and growth of Schwann cell and possessed good cyto-compatibility.

3.2. *In vitro*

3.2.1. *Determination of iron overload*

The Perl's staining showed that WD induced iron overload in the nerve (Fig. 2A). Compared with normal nerves, cultured nerves showed blue precipitates at 1 d. This blue iron deposition increased significantly at 3 d and decreased at 5 d. These phenomena are consistent with the

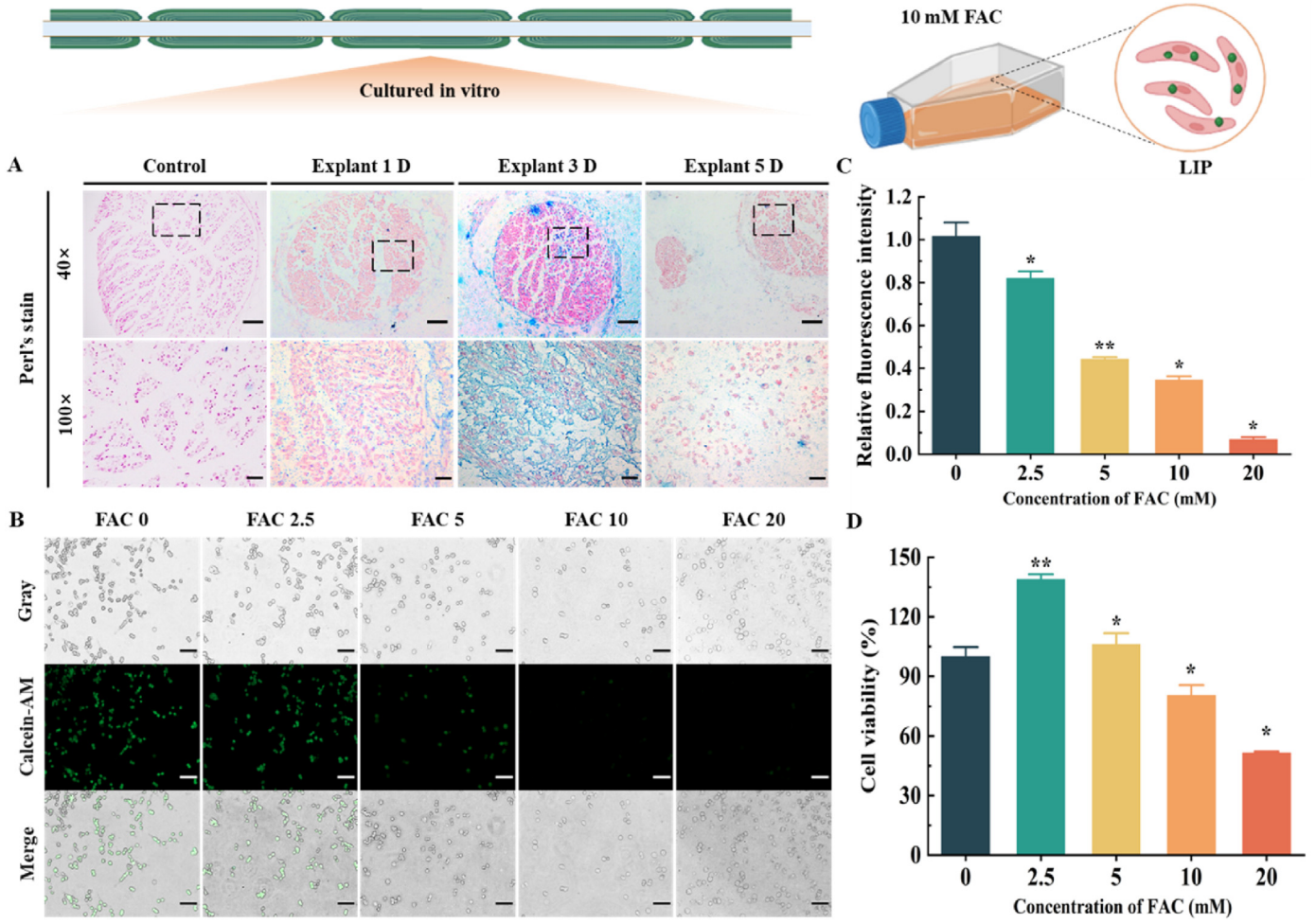

Fig. 2. Construction of *in vitro* model of iron overload. (A) Perl's staining of normal nerves and explant. (B) Morphology and labile iron pool of RSCs after treatment with FAC for 24 h. (C) Cell viability of RSCs was estimated CCK-8 (vs FAC 0). (D) Relative fluorescence intensity of RSCs (vs FAC 0). Data are means ± SD, n = 6, *P < 0.05, **P < 0.01.

results of the distribution of ferric iron in the nerve crush site [37]. The decrease in ferric iron is due to the up-regulation of the expression of transferrin and transferrin receptor, which allows Fe^{3+} to be transported into cells and converted to Fe^{2+} by the Fenton reaction [3]. Schwann cells are essential to WD, responsible for removing myelin and promoting the formation of the Büngner bands [29]. After treatment with FAC, RSCs lost antennae and changed from a spindle shape to a round shape (Fig. 2B). Meanwhile, the intracellular fluorescence intensity was significantly reduced after 10 mM FAC treatment, indicating the intracellular ferrous ion increase (Fig. 2C). The cell viability is about 80% in a 10 mM FAC solution. Referring to previous indicators [38,39], the 10 mM FAC solution was chosen to simulate the iron overload micro-environment *in vitro*.

3.2.2. DFO alleviated peroxidation, mitochondrial abnormalities and increased ROS caused by iron overload

The main mechanism of iron death is liposome peroxidation, which is reflected in the weakening of the antioxidant system [40]. The inactivation of GPX4 (antioxidant enzyme) based on the reduction of GSH was considered as the main manifestation of ferroptosis [41]. After pretreatment with 10 mM FAC, the content of GSH and the activity of GPX4 decreased significantly (Fig. 3B and C). In contrast, in the PDPLA/DFO group, the down-regulation of GSH was alleviated and GPX4 was reactivated (Fig. 3 A and B). The results indicated that DFO reversed the intracellular peroxidation induced by iron overload. Iron overload was deemed to cause mitochondrial dysfunction and inactivation of GPX4 induced mitochondria to produce ROS [42]. Normally, mitochondrial dysfunction is manifested in the decrease of its membrane potential. The harvested cells were double-stained with JC-1 and DAPI dyes, and MMP was evaluated by reading the ratio of red/green fluorescence intensity (Fig. 3D and F). After FAC treatment, JC-1 appeared green fluorescence and the red/green ratio decreased. In the presence of DFO, JC-1 displayed red and the red/green ratio increased. The results illustrated that iron overload induced abnormality of mitochondria, while the DFO alleviated the phenomenon. Iron overload caused a significant increase in ROS levels, which were about 7 times higher than the control group. However, ROS levels recovered in the PDPLA/DFO group. The results indicated that iron overload caused an increase in ROS, while DFO relieves symptoms (Fig. 3E and G). Iron overload induced GPX4 inactivation based on the reduction of GSH, followed by abnormal mitochondrial metabolism and increased ROS, and DFO was able to completely reverse it. Recent findings suggest that Schwann cells contribute to the delivery of iron to axonal mitochondria, required for proper nerve repair [43]. However, excessive iron obviously caused an increase in active oxygen. The continuously rising ROS in Schwann cells disrupts mitochondria, neuroenergetics and axon stability [44]. Obviously, DFO can restore the redox homeostasis of RSCs to promote cell survival, which is beneficial to nerve regeneration.

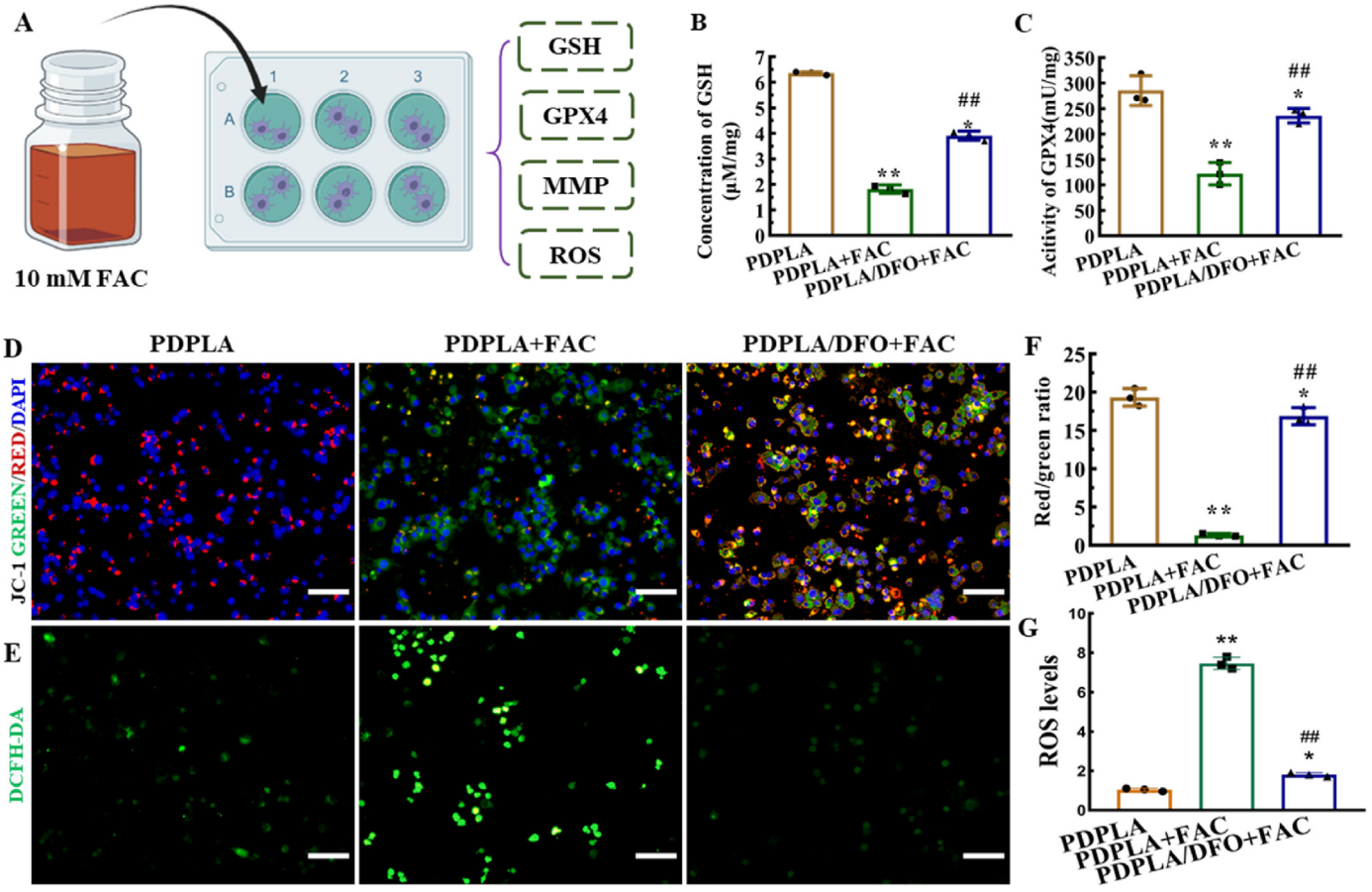

Fig. 3. Determination of GSH, GPX4, MMP and ROS under iron overload. (A) Seed cells on the membrane, then treat with FAC10. The microplate reader evaluated the intracellular GSH content (B) and GPX4 activity (C). DFO alleviated decrease in MMP. (D) And increase in ROS induced by Iron (E). Use image J to calculate JC 1 red/green ratio (F), and DCFH-DA fluorescence intensity (G) (Data are means ± SD, n = 3). Data are means ± SD, * vs PDPLA group, # vs PDPLA + FAC group, *p < 0.05, **p < 0.01; ##p < 0.01.

3.2.3. DFO inhibited apoptosis of ER and mitochondrial stress pathway caused by iron overload

In fact, researchers demonstrated that the way iron overload induces cell death is not only related to ferroptosis, but also to organelle-mediated apoptosis. The above results showed that iron overload caused an increase in the level of intracellular oxidation (accumulation of ROS). ROS is one of inducement of ER and mitochondrial stress [45,46]. The results showed that iron overload induced up-regulation of GPR78 (ER stress receptor) and Bax (mitochondrial-related pro-apoptotic factor) expression, while it is significantly reduced after DFO treatment (Fig. 4A and B). In addition, the expression of Bcl-2 (mitochondrial-related anti-apoptotic factor) decreased after FAC treatment (Fig. 4A). It was found that iron overload made the Bax/Bcl-2 ratio increase, while DFO recovered the ratio (Fig. 4B). After iron induction, the apoptotic rate increased to 60%, and decreased after DFO treatment (Fig. 4C and D). The results indicate that iron overload induces RSCs apoptosis through mediating ER and mitochondrial stress, while DFO alleviates the trend. In fact, it has been proved that proanthocyanidins can inhibit endoplasmic reticulum stress and restore Schwann cell damage in early diabetic peripheral neuropathy [47]. The function of mitochondria determined the vitality of Schwann cells [48]. In general, DFO relieved organelle stress, which could repair RSCs damage. Correlation analysis of the factors illustrated that iron overload induced mitochondrial abnormalities and further increased ROS by inducing a decrease in GSH and GPX4, which are responsible for apoptosis related to endoplasmic reticulum and mitochondrial (Figure S1).

3.3. In vivo

3.3.1. Histological investigation and ultrastructure observation of the distal portion after PNI

In the H&E staining, the axons, myelin sheaths and cells in the distal portion can be clearly observed (Fig. 5 A). In control group, myelinated nerve fibers are present as central dots; the pink axons are surrounded by an annulus of myelin sheath, which appears empty due to the extraction of lipids. Nerve fibers are closely arranged, and Schwann cells, which are dark purple in HE staining, are scattered around the axons. In PDPLA group, numerous inflammatory cells infiltrated the perineurium and invade the nerve. Compared with the PDPLA group, the nerve in the PDPLA/DFO group had less inflammatory infiltration. In autograft group, the shape and the number of nerve fibers were similar to those of normal nerves. The morphological deformation reduction of the myelin sheath in PDPLA group indicated neurodegeneration, which was similar to the PDPLA/DFO group (Fig. 5B and D). While the area of myelin sheath was reduced less in autograft group. Compared with the control group, WD appeared after nerve injury, which was mainly reflected in the deformation and reduction of myelin sheath (Fig. 5C and E). Ultrastructural illustrated the three major morphological variants of Wallerian degeneration: dark degeneration, watery degeneration and demyelination [49]. Among them, the myelin sheath of PDPLA group and PDPLA/DFO group were completely degenerated. While autograft group showed lighter WD. Martinez-Vivot R. et al. Proved that the iron content at the proximal stump was almost unchanged after injury, but increased

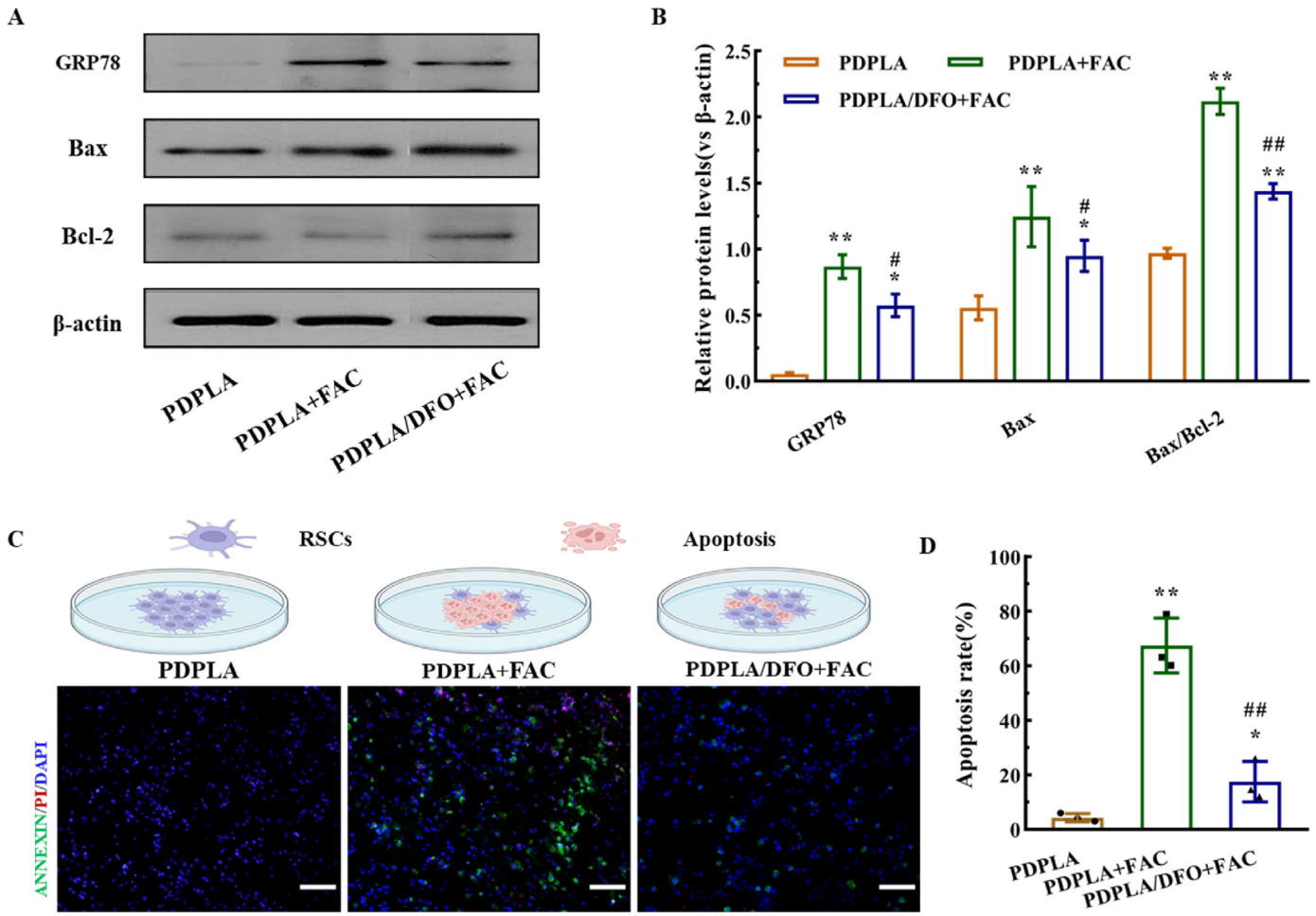

Fig. 4. DFO inhibits ER and mitochondrial-related apoptosis induced by iron overload. (A) Analysis of protein expression of GRP78, Bax and Bcl-2 by Western blot with β-actin as a reference. (B) Relative protein expression of GRP78, Bax and Bcl-2 (vs β-actin, n = 3). (C) ANNEXIN/PI fluorescent staining of apoptotic cells and DAPI staining of nuclei and (D) relative fluorescence intensity measurement (vs PDPLA, n = 3). Data are means ± SD, * vs PDPLA group, # vs PDPLA + FAC group, *p < 0.05, **p < 0.01; #p < 0.05, ##p < 0.05.

significantly at the distal stump [3]. Therefore, iron overload was probably caused by the rapid degeneration of axons.

Soon after peripheral nerve injury, WD of the distal nerve stump begins with the degeneration and disintegration of axons and the dedifferentiation of Schwann cells [50]. Schwann cells decompose myelin and recruit macrophages, which mediate the initial inflammatory response [50,51]. Obviously, the inflammatory response caused by PNI in the PDPLA group is more intense, but it can be effectively relieved after DFO loading. It was related to unique characteristics of DFO to down-regulate inflammation [26]. WD of PDPLA group and PDPLA/DFO group was more severe than that of autograft group. Actually, WD is also in favor of axonal regeneration, when providing a suitable microenvironment [52]. In summary, WD appeared at the distal stump accompanied by axon degeneration and inflammatory infiltration, While PDPLA/DFO nerve conduits could significantly reduce the inflammation.

3.3.2. Nerve conduits affect inflammation, and apoptosis of the distal stump

HO-1 catalyzes the decomposition of heme into biliverdin, carbon monoxide and ferrous iron. Overexpression of HO-1 produces excess ferrous iron [53,54]. In PDPLA group, HO-1 was overexpressed (about twice that of the control group), while the expression of HO-1 recovered in PDPLA/DFO group (Fig. 6B and C). It indicated that PDPLA/DFO alleviated iron overload during Wallerian Degeneration. The imbalance of iron homeostasis causes neuronal dysfunction, and iron accumulation causes a continuous pro-inflammatory environment [55]. According to morphological analysis, nerve respond differently to WD among groups. Compared with control group, the rate of CD68 positive cells, the expression of TNF-α, IL-1β all increased in PDPLA group, and IL-10 decreased (Fig. 6B and C). Comparing with the PDPLA group, it was found that inflammation declined in PDPLA/DFO group, which was mainly reflected in the reduction of macrophages, the down-regulation of pro-inflammatory factors (TNF-α, IL-1β) and the up-regulation of anti-inflammatory factors (IL-10). The relatively lower inflammatory response in PDPLA/DFO group was similar to that in autograft group. HO-1-dependent iron overload causes elevated levels of inflammatory markers, such as iNOS, p65, IL-1β, TNF-α, Caspase-1, and NLRP3, and administration of iron chelators ameliorated inflammation [56]. In addition, restoring iron metabolism favors the formation of an anti-inflammatory environment [57]. Thus, PDPLA/DFO conduits down-regulated the expression of TNF-α and IL-1β and up-regulated the expression of IL-10. In summary, PDPLA/DFO has the effect of alleviating the inflammation of the distal stump, achieving a microenvironment similar to that of autologous transplantation. The positive rate of TUNEL in PDPLA group was high (about 15%), while the apoptotic rate decreased (less than 2%) in PDPLA/DFO group (Fig. 6B and C). The recruitment of macrophages is due to the need to remove degenerated myelin, and both TNF-α and IL-1β play an important role in the period [58,59]. However, long-lasting inflammation is not conducive to tissue regeneration, and an anti-inflammatory environment (IL-10 promotes nerve regeneration and functional recovery [60]) is more suitable for cell

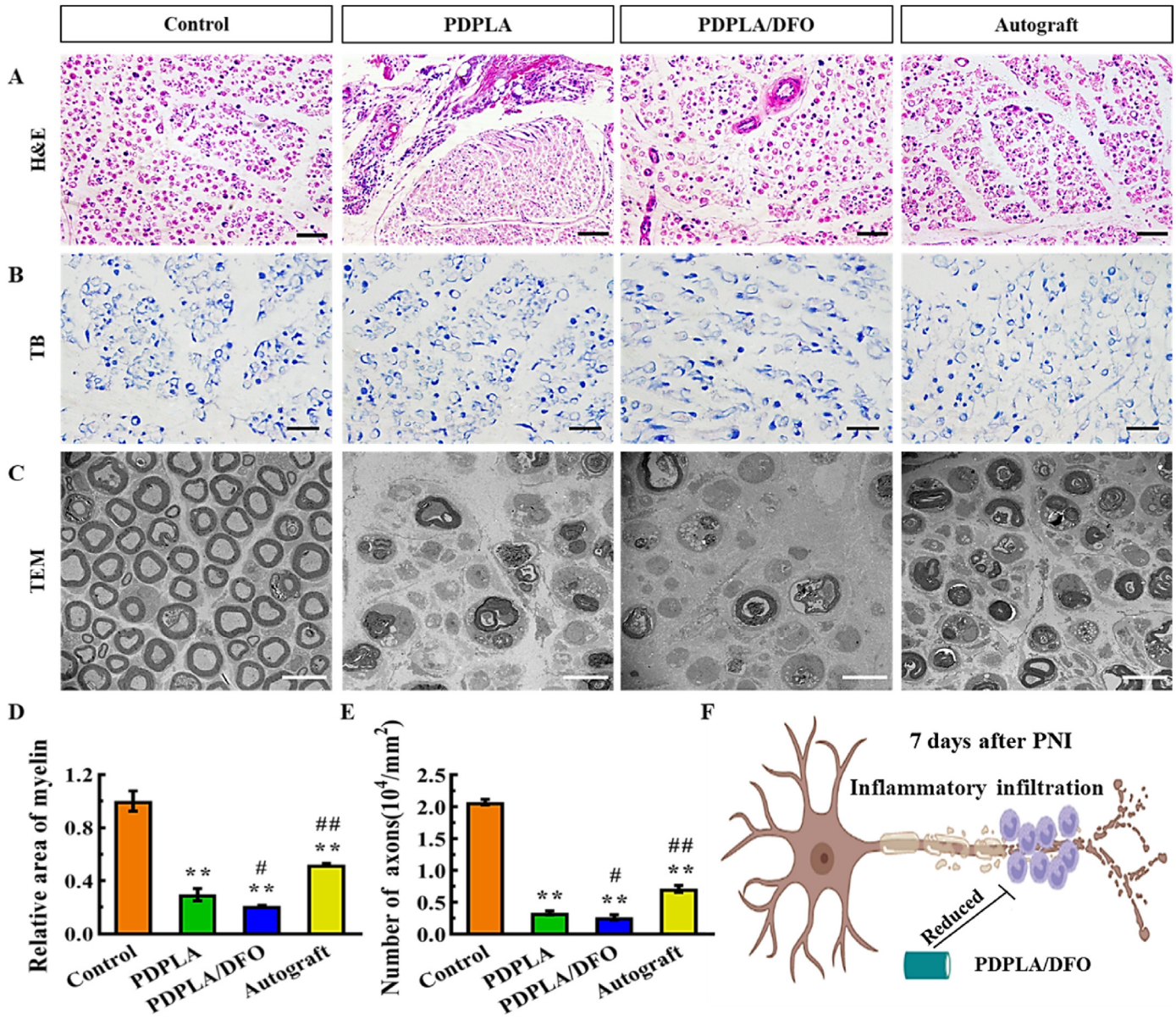

Fig. 5. Histological investigation and morphometric analysis using H&E staining (scale bar = 50 μm) (A), TB staining (scale bar = 50 μm)(B) and TEM (scale bar = 10 μm) (C). (D) The relative myelin area was calculated from the TB by image j (vs control). (E) Calculate the number of myelin sheaths per mm^2, (vs control). (F) PDPLA/DFO reduces inflammatory infiltration after nerve injury. Data are means ± SD, n = 3, * vs Control group, # vs PDPLA group, *P < 0.05, **P < 0.01; $^{\#}$P < 0.05, $^{\#\#}$P < 0.05.

growth. In PDPLA group, the entire distal end was still in the acute inflammatory phase, while PDPLA/DFO adjusted it to the anti-inflammatory phase. In addition, PDPLA/DFO was obviously more suitable for distal cell survival (lower apoptosis). In summary, the results illustrated that PDPLA/DFO provided an anti-inflammatory regenerative microenvironment and alleviated apoptosis.

3.3.3. *PDPLA/DFO relieves ER and mitochondrial stress after PNI*

In TEM observations, we found that the cells were breaking down the myelin sheath (Fig. 7A). In PDPLA group, the nucleus deformed, the number and volume of mitochondria increased, and the ER swelled. In the PDPLA/DFO group and autograft group, the morphology of mitochondria and ER remained normal. Previous studies have shown that ER and mitochondrial stress regulate tissue growth (e.g., skin repair, bone regeneration, tumor growth and nerve regeneration) [61–63]. Therefore, we analyzed the expression of proteins related to mitochondrial stress (Bax, BCL-2, Cyt-c) and ER stress (GRP78, CHOP, IRE-1α, XBP-1). The up-regulation of Bax (promoting apoptosis) and the down-regulation of BCL-2 (inhibiting apoptosis) stimulate the up-regulation Cyt-c (Fig. 7B). In addition, GRP78, CHOP, IRE-1a and XBP1 have significant high expressions in PDPLA group (Fig. 7C). In contrast, the expression of these proteins in PDPLA/DFO group and the autograft group show a decreasing trend. The results demonstrated that ER and mitochondrial stress were activated in PDPLA group, while inactivated in PDPLA/DFO group. In general, PDPLA/DFO relieves ER and mitochondrial stress after PNI.

Researchers proved that organelle stress were essential for regulating the micro-environment [64,65]. Distal axon degeneration produces damaged mitochondria, which releases harmful reactive oxygen species and initiate apoptotic signaling cascades [66]. Wang et al. provided important evidence that MANF expression might contribute to delayed corneal epithelial wound healing and impaired nerve regeneration by increasing ER stress [67]. Salaroglio et al. demonstrated that the adaptation to ER stress in cancer cells produced a MDR (multidrug resistance) phenotype and PERK/Nrf2/MRP1 axis is responsible for the resistance to

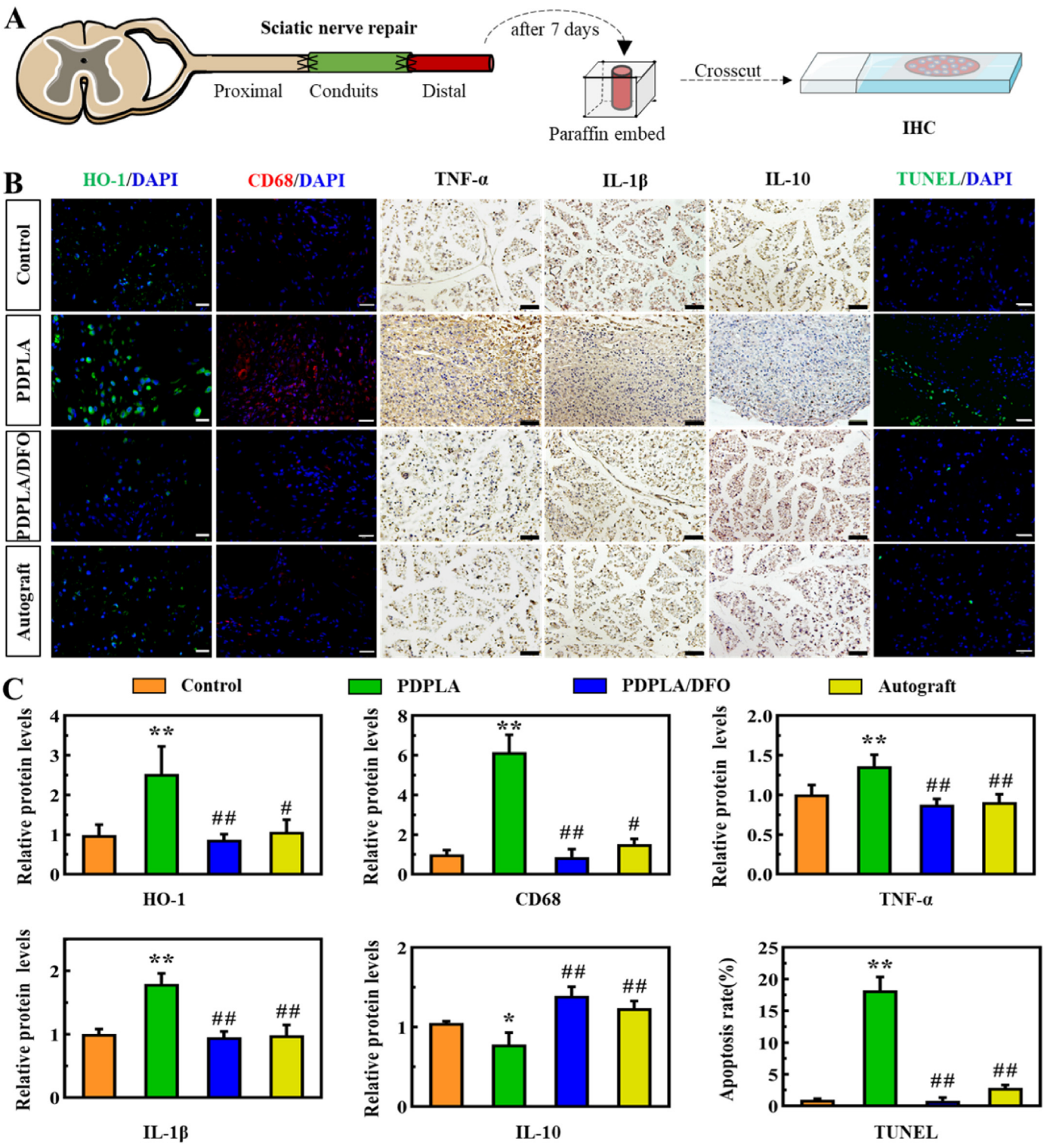

Fig. 6. Assess the microenvironment of the distal nerve. (A) Obtain cross sections of the distal stump. (B) Immunofluorescence of HO-1, CD68 (Scale bar = 20 μm); immunohistochemistry of TNF-α, IL-1β and IL10 (Scale bar = 50 μm); and TUNEL (Scale bar = 20 μm). (C) Semi-quantitative protein expression and measurement of apoptosis rate. Data are means ± SD, n = 3, * vs Control group, # vs PDPLA group, *p < 0.05, **p < 0.01; #p < 0.05, ##p < 0.05.

ER stress and chemotherapy, and might represent a good therapeutic target in aggressive and resistant tumors [68]. Besides, inflammation is crucial in the regeneration process, current research has revealed that ER stress can trigger an inflammatory response through diverse transducers of unfold protein reaction. In neurodegenerative diseases such as Alzheimer's disease, Parkinson's disease, and amyotrophic lateral sclerosis, tissue inflammation is associated with severe and persistent ER stress. Mitochondrial damage is also a key feature of inflammation. Lee et al. demonstrated the therapeutic effects of direct mitochondrial transplantation anti-inflammatory effects in tendinopathy [69]. Using 1

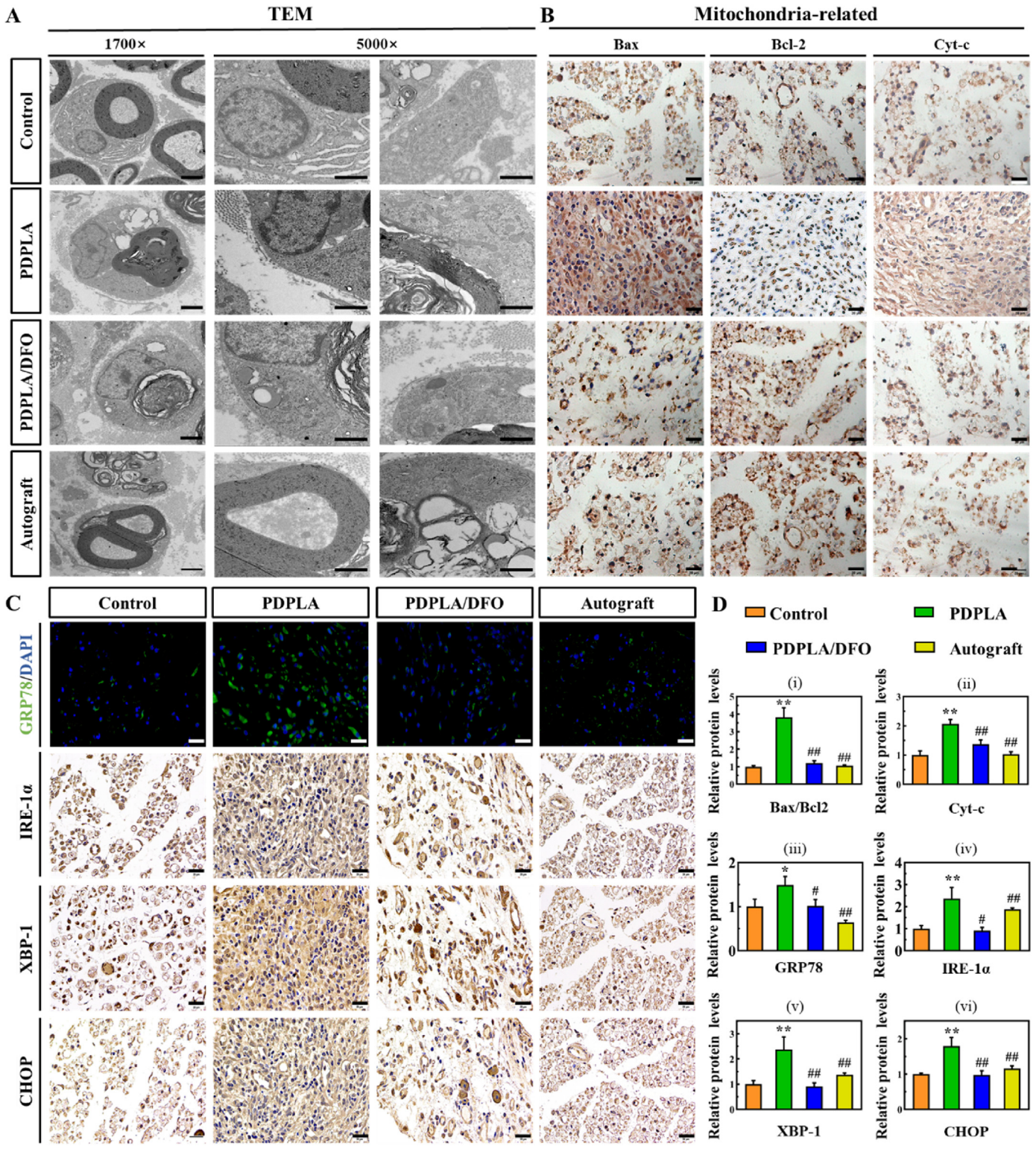

Fig. 7. PDPLA/DFO relieves ER and mitochondrial stress after PNI. (A) TEM images of the distal stump at 1700 × (Scale bar = 2 μm) and 5000 × (Scale bar = 1 μm). Immunohistochemical staining of (B) mitochondria-related protein: BAX, BCL2 and Cyt-C; and (C) ER-related protein: GRP78, CHOP, IRE-1α and XBP1(Scale bar = 50 μm). (D) Semi-quantitative analysis of (i) BAX/BCL2, (ii) Cyt-C, (iii) GRP78, (iv) CHOP, (v) IRE-1a, (vi) XBP. Data are means ± SD, n = 3, * vs Control group, # vs PDPLA group, *P < 0.05, **P < 0.01; #P < 0.05, ##P < 0.05.

mg/kg of Salubrinal, an ER stress inhibitor, to treat mice with Blast traumatic brain injury, significantly reduced iron accumulation and protected nerves [70]. High dietary iron mice revealed that ROS and mitochondrial-related apoptosis are exacerbated, which may be the cause of AD [71]. According to the correlation analysis, continuous iron overload activates organelle stress, resulting in a microenvironment that is not conducive to nerve growth (Figure S3). In present study, the PDPLA/DFO may first down-regulated the iron in local, and then reduced the ER and mitochondrial stress caused by WD, thereby alleviating nerve inflammation, apoptosis and oxidative stress.

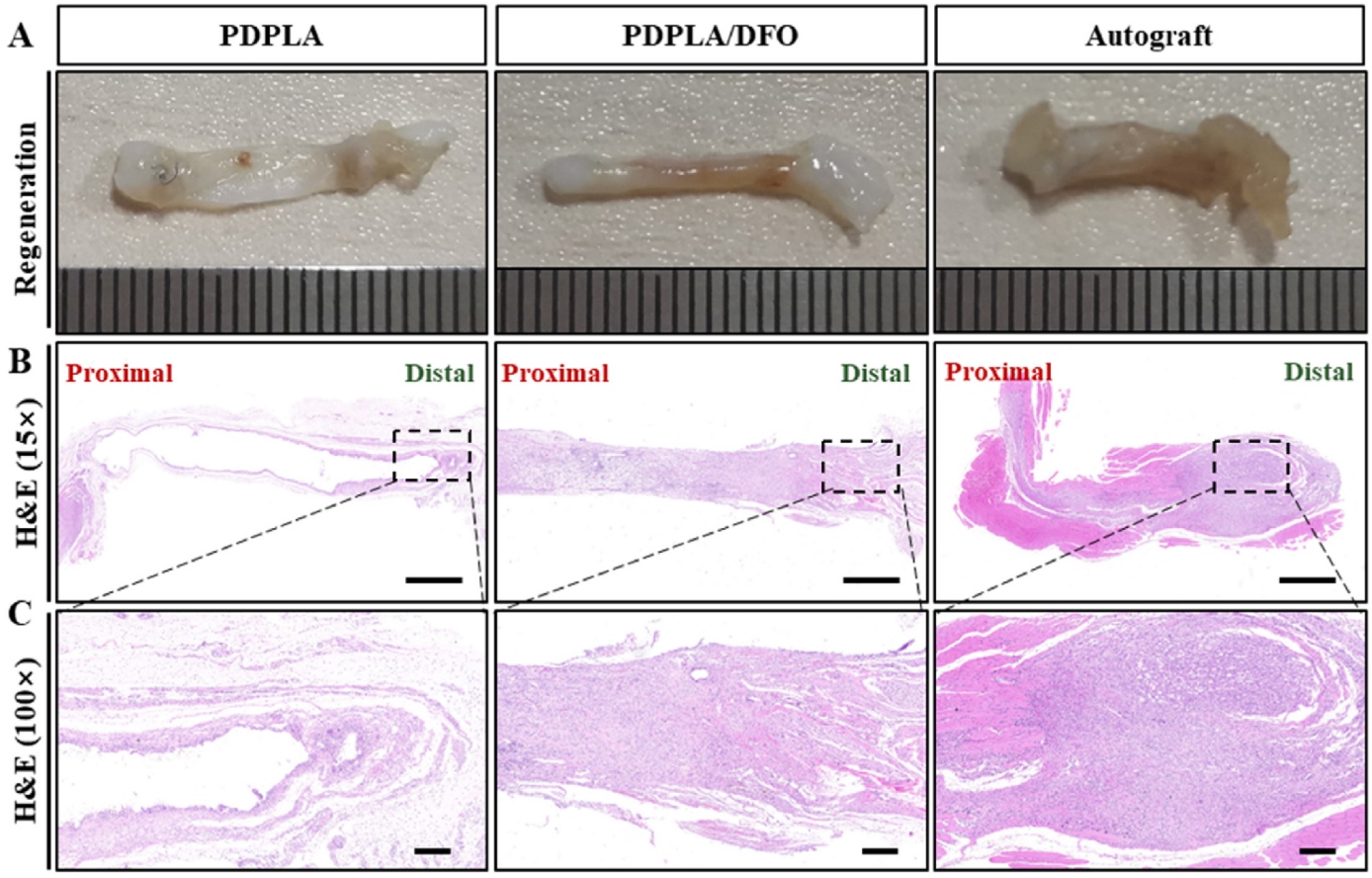

Fig. 8. PDPLA/DFO stimulated nerve regeneration. (A) Nerve repair in each group 4 weeks after PNI. H&E Stain of regenerating nerve, (B) 15 × (scale bar = 1 mm) and (C)100 × (scale bar = 100 μm).

3.4. PDPLA/DFO repaired sciatic nerve injury

Brain-derived neurotrophic factor (BDNF) and nerve growth factor (NGF) have significant effects on axon regeneration and Schwann cells proliferate [72,73]. Compared with the PDPLA group, the PDPLA/DFO group promoted the expression of BDNF and NGF, which was similar to the autograft group (Figure S2). The result indicated that PDPLA/DFO constructed a suitable microenvironment for regeneration. After 4 weeks of treatment of PNI with nerve conduits, nerves were harvested (Fig. 8). In autograft group, the nerves have grown intact, which were wrapped the epineurium and have a thicker diameter. In PDPLA/DFO group, the distal and proximal ends of the defect were connected, and the regeneration segment was filled with nerve cells. In PDPLA group, the regeneration segment was still vacant, and only the Büngner bands was formed. The results indicated that PDPLA/DFO promoted nerve regeneration. Four weeks after surgery, SFI of PDPLA group, PDPLA/DFO group and autograft were -55.25 ± 2.38, -46.26 ± 4.89 and -44.07 ± 3.08, respectively. Electrophysiological results: The nerve conduction velocities of PDPLA group, PDPLA/DFO group and autograft were 88.16 $\pm$ 13.18 m s-1, 105.48 $\pm$ 12.65 m s-1 and 106.52 $\pm$ 21.52 m s-1; the peak potentials were 10.94 $\pm$ 1.11 mV, 18.74 $\pm$ 2.73 mV and 19.3 $\pm$ 1.62 mV. These results indicate that PDPLA/DFO can promote the recovery of nerve function, and the effect is similar to that of autograft.

4. Conclusion

In this paper, we report that there is an iron overload in the microenvironment of the distal stump during PNI. Accordingly, we prepared a DFO-loaded poly(3(S)-methylmorpholine-2,5-diioned-*co*-lactone) conduits (PDPLA/DFO) by electrospinning to bridge the broken sciatic nerve in rats. *In vitro* model of iron-overloaded Schwann cells, the activated iron-overloaded responses was characterized with a decrease GSH content, an inactivation GPX4 activity and an increase in ROS content. Meanwhile, the endoplasmic reticulum stress, mitochondrial stress and apoptosis were observed, which was alleviated by the DFO. *In vivo*, it is obviously that the PDPLA/DFO greatly promoted the nerve regeneration, which eased both the ER and mitochondria stress induced by WD, and further improved the microenvironment of the distal stump (inhibition of pro-inflammation and alleviated apoptosis). In summary, iron-overload will destroy the microenvironment for peripheral nerve regeneration, by inducing the outbreak of ROS, and triggering the organelle stress, pro-inflammation and apoptosis. Therefore, relieving iron-overload is a promising therapy to facilitate the peripheral nerve regeneration.

Credit author statement

Lei Han;Visualization, Investigation, Writing – original draft Xianzhen Dong; Visualization, Investigation Tong Qiu;Supervision, Methodology, Writing- Reviewing and Editing Zhaona Dou; Investigation Lin Wu;Investigation Honglian Dai;Supervision, Funding acquisition

Supporting Information

Supporting Information is available from the Wiley Online Library or from the author.

Declaration of competing interest

The authors declare no conflict of interest.

Acknowledgements

This work was supported by grants from the National Key Research and Development Program of China (2016YFC1101605), the National Natural Science Foundation of China (51772233), the Major Special Project of Technological Innovation of Hubei Province (2019ACA130), and the Key Basic Research Program of Shenzhen (JCYJ20200109150218836).

Appendix A. Supplementary data

Supplementary data to this article can be found online at https://doi.org/10.1016/j.mtbio.2022.100387.

References

[1] A. Magaz, A. Faroni, J.E. Gough, et al., Bioactive silk-based nerve guidance conduits for augmenting peripheral nerve repair, Adv Healthc Mater 23 (2018), e1800308, https://doi.org/10.1002/adhm.201800308.
[2] C.R. Carvalho, W. Chang, J. Silva-Correia, et al., Tissue engineering: engineering silk fibroin-based nerve conduit with neurotrophic factors for proximal protection after peripheral nerve injury, Advanced Healthcare Materials 2 (2021), 2170003, https://doi.org/10.1002/adhm.202170003.
[3] R. Martinez-Vivot, G. Copello, M.C. Leal, et al., DMT1 iron uptake in the PNS: bridging the gap between injury and regeneration, Metallomics 12 (2015) 1612, https://doi.org/10.1039/c5mt90048d. -1612.
[4] J. Wu, J.J. Yang, Y. Cao, et al., Iron overload contributes to general anaesthesia-induced neurotoxicity and cognitive deficits, J. Neuroinflammation 1 (2020) 110, https://doi.org/10.1186/s12974-020-01777-6.
[5] L.W. Powell, L. Summerville, D.J. Cullen, et al., Effect of hemochromatosis genotype and lifestyle factors on iron and red cell indices in a community population, Clin. Chem. 2 (2001) 202–208, https://doi.org/10.1093/clinchem/47.2.202.
[6] C.D. Obi, T. Bhuiyan, H.A. Dailey, et al., Ferrochelatase: mapping the intersection of iron and porphyrin metabolism in the mitochondria, Front. Cell Dev. Biol. (2022), 894591, https://doi.org/10.3389/fcell.2022.894591.
[7] Y. Li, X. Huang, J. Wang, et al., Regulation of iron homeostasis and related diseases, Mediat. Inflamm. (2020), 6062094, https://doi.org/10.1155/2020/6062094.
[8] H. Kawabata, Transferrin and transferrin receptors update, Free Radic. Biol. Med. (2019) 46–54, https://doi.org/10.1016/j.freeradbiomed.2018.06.037.
[9] E. Corradini, E. Buzzetti, A. Pietrangelo, Genetic iron overload disorders, Mol. Aspect. Med. (2020), 100896, https://doi.org/10.1016/j.mam.2020.100896.
[10] X. Jing, Q. Wang, T. Du, et al., Calcium chelator BAPTAAM protects against iron overloadinduced chondrocyte mitochondrial dysfunction and cartilage degeneration, Int. J. Mol. Med. 4 (2021), https://doi.org/10.3892/ijmm.2021.5029.
[11] J. Che, H. Lv, J. Yang, et al., Iron overload induces apoptosis of osteoblast cells via eliciting ER stress-mediated mitochondrial dysfunction and p-eIF2alpha/ATF4/CHOP pathway in vitro, Cell. Signal. (2021), 110024, https://doi.org/10.1016/j.cellsig.2021.110024.
[12] G.C. Chan, S.Y. Ha, Y.F. Cheung, et al., Iron-overload induces apoptosis in cardiomyocytes and hepatocytes via mitochondrial/caspase-3 pathways, Blood 11 (2008) 1872, https://doi.org/10.1182/blood.V112.11.1872.1872. -1872.
[13] Q. Wang, H. Cai, Z. Hu, et al., Loureirin B promotes axon regeneration by inhibiting endoplasmic reticulum stress: induced mitochondrial dysfunction and regulating the akt/GSK-3beta pathway after spinal cord injury, J. Neurotrauma 12 (2019) 1949–1964, https://doi.org/10.1089/neu.2018.5966.
[14] F. Wu, K. Xu, L. Liu, et al., Vitamin B12 enhances nerve repair and improves functional recovery after traumatic brain injury by inhibiting ER stress-induced neuron injury, Front. Pharmacol. (2019) 406, https://doi.org/10.3389/fphar.2019.00406.
[15] A. Loreto, C.S. Hill, V.L. Hewitt, et al., Mitochondrial impairment activates the Wallerian pathway through depletion of NMNAT2 leading to SARM1-dependent axon degeneration, Neurobiol. Dis. (2020), 104678, https://doi.org/10.1016/j.nbd.2019.104678.
[16] C. Zhao, D. Yu, Z. He, et al., Endoplasmic reticulum stress-mediated autophagy activation is involved in cadmium-induced ferroptosis of renal tubular epithelial cells, Free Radic. Biol. Med. (2021) 236–248, https://doi.org/10.1016/j.freeradbiomed.2021.09.008.
[17] D.G. Lee, M.K. Kam, K.M. Kim, et al., Peroxiredoxin 5 prevents iron overload-induced neuronal death by inhibiting mitochondrial fragmentation and endoplasmic reticulum stress in mouse hippocampal HT-22 cells, Int. J. Biochem. Cell Biol. (2018) 10–19, https://doi.org/10.1016/j.biocel.2018.06.005.
[18] Y. Qian, H. Lin, Z. Yan, et al., Functional nanomaterials in peripheral nerve regeneration: scaffold design, chemical principles and microenvironmental remodeling, Mater. Today (2021) 165–187, https://doi.org/10.1016/j.mattod.2021.09.014.
[19] Y. Qian, Y. Cheng, Y. Ouyang, et al., Multilayered spraying and gradient dotting of nanodiamond–polycaprolactone guidance channels for restoration of immune homeostasis, NPG Asia Mater. 1 (2019), https://doi.org/10.1038/s41427-019-0136-8.
[20] Y. Qian, Q. Han, X. Zhao, et al., 3D melatonin nerve scaffold reduces oxidative stress and inflammation and increases autophagy in peripheral nerve regeneration, J. Pineal Res. 4 (2018), e12516, https://doi.org/10.1111/jpi.12516.
[21] S. Rotshenker, Wallerian degeneration: the innate-immune response to traumatic nerve injury, J. Neuroinflammation (2011) 109, https://doi.org/10.1186/1742-2094-8-109.
[22] G. Esposito, E. Capoccia, F. Turco, et al., Palmitoylethanolamide improves colon inflammation through an enteric glia/toll like receptor 4-dependent PPAR-alpha activation, Gut 8 (2014) 1300–1312, https://doi.org/10.1136/gutjnl-2013-305005.
[23] Y. Feng, W. Lu, X. Ren, et al., Electrospun poly(lactide-co-glycolide-co-3(S)-methyl-morpholine-2,5-dione) nanofibrous scaffolds for tissue engineering, Polymers 2 (2016), https://doi.org/10.3390/polym8020013.
[24] X. Dong, P. Wu, L. Yan, et al., Oriented nanofibrous P(MMD-co-LA)/Deferoxamine nerve scaffold facilitates peripheral nerve regeneration by regulating macrophage phenotype and revascularization, Biomaterials (2022) 121–288, https://doi.org/10.1016/j.biomaterials.2021.121288.
[25] K. Ghosal, R. Augustine, A. Zaszczynska, et al., Novel Drug Delivery Systems Based on Triaxial Electrospinning Based Nanofibers, Reactive and Functional Polymers, 2021, https://doi.org/10.1016/j.reactfunctpolym.2021.104895.
[26] P. Holden, L.S. Nair, Deferoxamine: an angiogenic and antioxidant molecule for tissue regeneration, Tissue Eng. B Rev. 6 (2019) 461–470, https://doi.org/10.1089/ten.TEB.2019.0111.
[27] S. Guo, G. Liu, D.M. Frazer, et al., Polymeric nanoparticles enhance the ability of deferoxamine to deplete hepatic and systemic iron, Nano Lett. 9 (2018) 5782–5790, https://doi.org/10.1021/acs.nanolett.8b02428.
[28] Y. Li, K. Pan, L. Chen, et al., Deferoxamine regulates neuroinflammation and iron homeostasis in a mouse model of postoperative cognitive dysfunction, J. Neuroinflammation 1 (2016) 268, https://doi.org/10.1186/s12974-016-0740-2. -268.
[29] J.M. Hendry, M.C. Alvarez-Veronesi, E. Placheta, et al., ErbB2 blockade with Herceptin (trastuzumab) enhances peripheral nerve regeneration after repair of acute or chronic peripheral nerve injury, Ann. Neurol. 1 (2016) 112–126, https://doi.org/10.1002/ana.24688.
[30] S. Song, K.W. McConnell, D. Amores, et al., Electrical stimulation of human neural stem cells via conductive polymer nerve guides enhances peripheral nerve recovery, Biomaterials (2021) 120–982, https://doi.org/10.1016/j.biomaterials.2021.120982.
[31] L. Zhang, X. Zou, B. Zhang, et al., Label-free imaging of hemoglobin degradation and hemosiderin formation in brain tissues with femtosecond pump-probe microscopy, Theranostics 15 (2018) 4129–4140, https://doi.org/10.7150/thno.26946.
[32] D.P. Perl, P.F. Good, Comparative techniques for determining cellular iron distribution in brain tissues, Ann. Neurol. (1992) S76–S81, https://doi.org/10.1002/ana.410320713.
[33] E.C. Jensen, Quantitative analysis of histological staining and fluorescence using ImageJ, Anat. Rec. 3 (2013) 378–381, https://doi.org/10.1002/ar.22641.
[34] L. Gao, QSIM, Quantitative structured illumination microscopy image processing in ImageJ, Biomed. Eng. Online (2015) 4, https://doi.org/10.1186/1475-925X-14-4.
[35] M. Zhao, M. Li, Y. Zheng, et al., Identification and analysis of a prognostic ferroptosis and iron-metabolism signature for esophageal squamous cell carcinoma, J. Cancer 5 (2022) 1611–1622, https://doi.org/10.7150/jca.68568.
[36] B.T. David, J.J. Curtin, J.L. Brown, et al., Treatment with hypoxia-mimetics protects cultured rat Schwann cells against oxidative stress-induced cell death, Glia 9 (2021) 2215–2234, https://doi.org/10.1002/glia.24019.
[37] G. Raivich, M.B. Graeber, J. Gehrmann, et al., Transferrin receptor expression and iron uptake in the injured and regenerating rat sciatic nerve, Eur. J. Neurosci. 10 (1991) 919–927, https://doi.org/10.1111/j.1460-9568.1991.tb00027.x.
[38] S. Lu, Y. Song, R. Luo, et al., Ferroportin-dependent iron homeostasis protects against oxidative stress-induced nucleus pulposus cell ferroptosis and ameliorates intervertebral disc degeneration in vivo, Oxid. Med. Cell. Longev. (2021), 6670497, https://doi.org/10.1155/2021/6670497.
[39] X. Jing, T. Du, T. Li, et al., The detrimental effect of iron on OA chondrocytes: importance of pro-inflammatory cytokines induced iron influx and oxidative stress, J. Cell Mol. Med. 12 (2021) 5671–5680, https://doi.org/10.1111/jcmm.16581.
[40] D. Chen, Z. Fan, M. Rauh, et al., ATF4 promotes angiogenesis and neuronal cell death and confers ferroptosis in a xCT-dependent manner, Oncogene 40 (2017) 5593–5608, https://doi.org/10.1038/onc.2017.146.
[41] B.R. Stockwell, J.P. Friedmann Angeli, H. Bayir, et al., Ferroptosis: a regulated cell death nexus linking metabolism, Redox Biology, and Disease, Cell 2 (2017) 273–285, https://doi.org/10.1016/j.cell.2017.09.021.
[42] F. Basit, L.M. van Oppen, L. Schockel, et al., Mitochondrial complex I inhibition triggers a mitophagy-dependent ROS increase leading to necroptosis and ferroptosis in melanoma cells, Cell Death Differ. 3 (2017) e2716, https://doi.org/10.1038/cddis.2017.133. -e2716.
[43] B.S. Mietto, P. Jhelum, K. Schulz, et al., Schwann cells provide iron to axonal mitochondria and its role in nerve regeneration, J. Neurosci. 34 (2021) 7300–7313, https://doi.org/10.1523/JNEUROSCI.0900-21.2021.
[44] L. Jia, M. Liao, A. Mou, et al., Rheb-regulated mitochondrial pyruvate metabolism of Schwann cells linked to axon stability, Dev. Cell 21 (2021) 2980–2994, https://doi.org/10.1016/j.devcel.2021.09.013.
[45] A. Guidarelli, M. Fiorani, L. Cerioni, et al., Arsenite induces DNA damage via mitochondrial ROS and induction of mitochondrial permeability transition, Biofactors 5 (2017) 673–684, https://doi.org/10.1002/biof.1375.
[46] A.P. Lightfoot, R.S. Morgan, R.G. Cooper, FRI0241 HMGB1 induces reactive oxygen species (ROS)-Dependent activation of the ER stress pathway in C2C12 myotubes,

Annals of the Rheumatic Diseases Suppl 2 (2016) 521, https://doi.org/10.1136/annrheumdis-2016-eular.2951, 521-521.
[47] Y. Ding, X. Dai, Z. Zhang, et al., Proanthocyanidins protect against early diabetic peripheral neuropathy by modulating endoplasmic reticulum stress, J. Nutr. Biochem. 7 (2014) 765–772, https://doi.org/10.1016/j.jnutbio.2014.03.007.
[48] B. He, F. Wu, L. Fan, et al., Carboxymethylated chitosan protects Schwann cells against hydrogen peroxide-induced apoptosis by inhibiting oxidative stress and mitochondria dependent pathway, Eur. J. Pharmacol. (2018) 48–56, https://doi.org/10.1016/j.ejphar.2018.02.024.
[49] S.K. Saggu, H.P. Chotaliya, P.C. Blumbergs, et al., Wallerian-like axonal degeneration in the optic nerve after excitotoxic retinal insult: an ultrastructural study, BMC Neurosci. (2010) 97, https://doi.org/10.1186/1471-2202-11-97.
[50] A.D. Gaudet, P.G. Popovich, M.S. Ramer, Wallerian degeneration: gaining perspective on inflammatory events after peripheral nerve injury, J. Neuroinflammation (2011) 110, https://doi.org/10.1186/1742-2094-8-110. -110.
[51] J.A. Fissel, M.H. Farah, The influence of BACE1 on macrophage recruitment and activity in the injured peripheral nerve, J. Neuroinflammation 1 (2021) 71, https://doi.org/10.1186/s12974-021-02121-2. -71.
[52] A.D. Gaudet, P.G. Popovich, M.S. Ramer, Wallerian degeneration: gaining perspective on inflammatory events after peripheral nerve injury, J. Neuroinflammation (2011) 110, https://doi.org/10.1186/1742-2094-8-110.
[53] W. Liao, W. Yang, Z. Shen, et al., Heme oxygenase-1 regulates ferrous iron and Foxo1 in control of hepatic gluconeogenesis, Diabetes 3 (2021) 696–709, https://doi.org/10.2337/db20-0954.
[54] M. Kim, H. Kim, D. Kim, et al., Heme oxygenase 1 in Schwann cells regulates peripheral nerve degeneration against oxidative stress, ASN Neuro (2019), 1759091419838949, https://doi.org/10.1177/1759091419838949.
[55] T.S. Zimmer, B. David, D.W.M. Broekaart, et al., Seizure-mediated iron accumulation and dysregulated iron metabolism after status epilepticus and in temporal lobe epilepsy, Acta Neuropathol. 4 (2021) 729–759, https://doi.org/10.1007/s00401-021-02348-6.
[56] C. Fernandez-Mendivil, E. Luengo, P. Trigo-Alonso, et al., Protective role of microglial HO-1 blockade in aging: implication of iron metabolism, Redox Biol. (2021), 101789, https://doi.org/10.1016/j.redox.2020.101789.
[57] Q. Mu, L. Chen, X. Gao, et al., The role of iron homeostasis in remodeling immune function and regulating inflammatory disease, Sci. Bull. 17 (2021) 1806–1816, https://doi.org/10.1016/j.scib.2021.02.010.
[58] A.B. Aurora, E.N. Olson, Immune modulation of stem cells and regeneration, Cell Stem Cell 1 (2014) 14–25, https://doi.org/10.1016/j.stem.2014.06.009.
[59] E.F. Lim, V. Hoghooghi, K.M. Hagen, et al., Presence and activation of pro-inflammatory macrophages are associated with CRYAB expression in vitro and after peripheral nerve injury, J. Neuroinflammation 1 (2021) 82, https://doi.org/10.1186/s12974-021-02108-z.
[60] B. Siqueira Mietto, A. Kroner, E.I. Girolami, et al., Role of IL-10 in resolution of inflammation and functional recovery after peripheral nerve injury, J. Neurosci. 50 (2015) 16431–16442, https://doi.org/10.1523/JNEUROSCI.2119-15.2015.
[61] T. Lou, J. Ma, Y. Xie, et al., Nuanxin capsule enhances cardiac function by inhibiting oxidative stress-induced mitochondrial dependent apoptosis through AMPK/JNK signaling pathway, Biomed. Pharmacother. (2021) 111188, https://doi.org/10.1016/j.biopha.2020.111188. -111188.
[62] A.O. Abdel-Zaher, R.B. Abd-Ellatief, N.A. Aboulhagag, et al., The potential relationship between gasotransmitters and oxidative stress, inflammation and apoptosis in lead-induced hepatotoxicity in rats, Tissue Cell (2021) 101511, https://doi.org/10.1016/j.tice.2021.101511. -101511.
[63] L. Cui, Q. Zhou, X. Zheng, et al., Mitoquinone attenuates vascular calcification by suppressing oxidative stress and reducing apoptosis of vascular smooth muscle cells via the Keap1/Nrf2 pathway, Free Radic. Biol. Med. (2020) 23–31, https://doi.org/10.1016/j.freeradbiomed.2020.09.028.
[64] M. Dong, X.Z. Xiao, Z.G. Su, et al., Light-induced ROS generation and 2-DG-activated endoplasmic reticulum stress by antitumor nanosystems: an effective combination therapy by regulating the tumor microenvironment, Small 17 (2019), e1900212, https://doi.org/10.1002/smll.201900212.
[65] K. Murakami, D. Kurotaki, W. Kawase, et al., Regulation of mitophagy by O-linked N-acetylglucosamine transferase is essential for hematopoietic stem cell maintenance, Blood Supplement 1 (2018) 171, https://doi.org/10.1182/blood-2018-171. -171.
[66] C. Sievers, N. Platt, V.H. Perry, et al., Neurites undergoing Wallerian degeneration show an apoptotic-like process with annexin V positive staining and loss of mitochondrial membrane potential, Neurosci. Res. 2 (2003) 161–169, https://doi.org/10.1016/s0168-0102(03)00039-7.
[67] X. Wang, W. Li, Q. Zhou, et al., MANF promotes diabetic corneal epithelial wound healing and nerve regeneration by attenuating hyperglycemia-induced endoplasmic reticulum stress, Diabetes 6 (2020) 1264–1278, https://doi.org/10.2337/db19-0835.
[68] I.C. Salaroglio, E. Panada, E. Moiso, et al., PERK induces resistance to cell death elicited by endoplasmic reticulum stress and chemotherapy, Mol. Cancer 1 (2017) 91, https://doi.org/10.1186/s12943-017-0657-0.
[69] J.M. Lee, J.W. Hwang, M.J. Kim, et al., Mitochondrial transplantation modulates inflammation and apoptosis, Alleviating Tendinopathy Both In Vivo and In Vitro, Antioxidants (Basel) 5 (2021) 696, https://doi.org/10.3390/antiox10050696. -696.
[70] B.P. Lucke-Wold, A.F. Logsdon, R.C. Turner, et al., Endoplasmic reticulum stress modulation as a target for ameliorating effects of Blast induced traumatic brain injury, J. Neurotrauma S1 (2017) S62–S70, https://doi.org/10.1089/neu.2016.4680.
[71] L.B. Li, R. Chai, S. Zhang, et al., Iron exposure and the cellular mechanisms linked to neuron degeneration in adult mice, Cells 2 (2019) 198, https://doi.org/10.3390/cells8020198. - 198.
[72] R. Li, Y. Li, Y. Wu, et al., Heparin-Poloxamer Thermosensitive Hydrogel Loaded with bFGF and NGF Enhances Peripheral Nerve Regeneration in Diabetic Rats, Biomaterials, 2018, pp. 24–37, https://doi.org/10.1016/j.biomaterials.2018.03.044.
[73] Y. Jiang, J.M. Fay, C.D. Poon, et al., Nanoformulation of brain-derived neurotrophic factor with target receptor-triggered-release in the central nervous system, Adv. Funct. Mater. 6 (2018), https://doi.org/10.1002/adfm.201703982.